Physics of the Earth and Planetary Interiors 173 (2009) 17–32

Contents lists available at ScienceDirect

Physics of the Earth and Planetary Interiors

journal homepage: www.elsevier.com/locate/pepi

Multiple resolution seismic attenuation imaging at Mt. Vesuvius

Luca De Siena, Edoardo Del Pezzo*, Francesca Bianco, Anna Tramelli

Istituto Nazionale di Geofisica e Vulcanologia, sezione di Napoli Osservatorio Vesuviano, Via Diocleziano, 328, 80124 Napoli, Italy

ARTICLE INFO

Article history:
Received 5 November 2007
Received in revised form 27 May 2008
Accepted 19 October 2008

Keywords:
Attenuation tomography
Mt. Vesuvius
Coda normalization method
Spectral slope
Multi resolution inversion

ABSTRACT

A three-dimensional *S* wave attenuation tomography of Mt. Vesuvius has been obtained with multiple measurements of coda-normalized *S*-wave spectra of local small magnitude earthquakes. We used 6609 waveforms, relative to 826 volcano-tectonic earthquakes, located close to the crater axis in a depth range between 1 and 4 km (below the sea level), recorded at seven 3-component digital seismic stations. We adopted a two-point ray-tracing; rays were traced in an high resolution 3-D velocity model. The spatial resolution achieved in the attenuation tomography is comparable with that of the velocity tomography (we resolve 300 m side cubic cells). We statistically tested that the results are almost independent from the radiation pattern. We also applied an improvement of the ordinary spectral-slope method to both *P*- and *S*-waves, assuming that the differences between the theoretical and the experimental high frequency spectral-slope are only due to the attenuation effects. Consequently we could check the coda-normalization method also comparing the *S* attenuation image with the *P* attenuation image. The images were obtained inverting the spectral data with a multiple resolution approach. Results have shown the general coincidence of low attenuation with high velocity zones. The joint interpretation of velocity and attenuation images allows us to interpret the low attenuation zone intruding toward the surface until a depth of 500 m below the sea level as related to the residual part of solidified magma from the last eruption. In the depth range between −700 and −2300 images are consistent with the presence of multiple acquifer layers. No evidence of magma patches greater than the minimum cell dimension (300 m) has been found. A shallow *P* wave attenuation anomaly (beneath the southern flank of the volcano) is consistent with the presence of gas saturated rocks. The zone characterized by the maximum seismic energy release cohincides with a high attenuation and low velocity volume, interpreted as a cracked medium.

1. Introduction

The knowledge of the internal structure of the volcanoes represents a crucial task to properly constrain the physical models of eruption. Passive tomography is one of the easiest and cheapest way to achieve this goal and is consequently widely applied for the study of volcano structures at several depths (Chouet, 1996).

There are two main factors limiting the maximum resolution that can be obtained in passive methods: the ray coverage and the wavelength of the waveforms from which the observables are retrieved. The first factor is linked to the station density and the source space distribution. The second is directly associated with the kind of events that are used as input. For a local tomography on a volcano with a volume of the order of 10 km of linear dimensions, local VT earthquakes, with their associate wavelengths that ordinary span from some kilometers to hundreds of meters (Chouet, 2003) are a suitable input. Generally the smallest wavelength characterizes the minimum cell size, and this can be considered as the thumb rule for this constraint. Moreover, to reach this minimum cell size, one needs a suitable source space distribution (sources as much as possible uniformly distributed in the volume, and an as dense as possible network of receivers). In a configuration typical of an up-to-date seismic network, an order of resolution of 300 m can be reached only in the volume cells with a sufficient ray coverage (Chouet, 1996). This leads to the solution of a mixed-determined problem, with an highly overdetermined system of equations correspondent to the cells with a redundant number of rays crossing through, and an equal- or lower-determined system for the other cells. A way to optimize the problem is to use an approach with a non uniform cell size, that maintains a sufficient over-determination in any cell, but reaches a good resolution only in the parts of the investigated volume characterized by the maximum ray coverage. This kind of approach is typically named as multi-step or multiple-resolution method (see Bai and Greenhalgh, 2005, for an example of travel time multi-step tomography on a volcano).

* Corresponding author. Fax: +39 081 6108323.
E-mail address: delpezzo@ov.ingv.it (E. Del Pezzo).

0031-9201/$ – see front matter © 2008 Elsevier B.V. All rights reserved.
doi:10.1016/j.pepi.2008.10.015

The attenuation of elastic waves depends strongly on a number of factors affecting the lithology, the most important of which are probably the temperature and the presence of fractures and hydrothermal or magmatic fluids. Attenuation is quantified by the quality factor, Q, defined as the ratio between the energy lost by a wave cycle and the energy of the cycle itself; equivalently, attenuation can be defined through the attenuation coefficient $\alpha = \pi f r / v Q$ that accounts for the damping of the wave amplitude, A, as a function of distance, r and frequency, f. This factor may greatly vary for rocks with the same composition but different degree of fracturing and/or temperature. The response of the rocks to the propagation of longitudinal and shear waves is different; the independent determination of the quality factors for longitudinal (Q_p) and shear (Q_s) waves, critical parameters for the characterization of the physical state of the rocks within a volcano, aims at discriminating between melt fluids and gases residing at shallow depths in the earth's crust. For this purpose, a comparative study of velocity and attenuation tomography can be critical (Hansen et al., 2004).

A phenomenon that intensely affects the wave propagation in volcanic areas is the scattering process, which tends to transfer the high-frequency energy of direct P and S waves into the coda of the seismograms (Sato and Fehler, 1998). Scattering is produced by the interaction of the wavefield with the small scale heterogeneities in the elastic parameters, as, for example, those associated with intense rock fracturing. The average attenuation caused by scattering, can be studied independently from the one caused by intrinsic attenuation, separating the two different types of losses (Bianco et al., 1999). Results on volcanoes show that, for frequencies higher than 10 Hz, scattering attenuation is more important than intrinsic attenuation (Del Pezzo et al., 2006a). For a comprehensive summary of results from attenuation measurements by a range of methods, at varying frequency, on different scales and in different geological settings the reader is referred to Sato and Fehler (1998).

Unfortunately, for the single path estimates (necessary for tomography) of the attenuation coefficient, the separation between the two kinds of contribution (scattering and intrinsic) is practically impossible. Consequently, in the attenuation tomography, the parameter obtained by the inversion is the total-Q or the correspondent attenuation coefficient.

This paper is aimed at giving an image of the shallow crust materials at Mt. Vesuvius volcanic area using shear wave attenuation tomography at high frequency (in the range between 10 and 20 Hz), solved with a multi-resolution method with a minimum cell (the greatest available resolution) of 300 m. Observables (total-Q inverse for each single path) are obtained using the coda-normalization method (Aki, 1980), and checked with the ordinary spectral-slope method. Spectral slope is used also to estimate P-wave total Q-inverse. Attenuation images are eventually compared with high resolution passive velocity tomography (the same minimum cell size, Scarpa et al., 2002). The images obtained with this method are also compared with those obtained at a resolution of 900 m in a previous study of the same area, carried out using a subset of the present data set (Del Pezzo et al., 2006b). We will show that the low attenuation zone located under the crater is coincident with a high velocity volume, possibly associated with residual frozen magma from the last eruptions; and that a high attenuation volume at 1–2 km of depth is coincident with a low velocity zone. This is interpreted as the aquifer permeating the shallow structure of Mt. Vesuvius.

2. Geological and seismological settings

Mt. Vesuvius is a stratovolcano formed by an ancient caldera (Mt. Somma) and by a younger volcanic cone (Mt. Vesuvius). The volcanic activity is dated back to 300–500 ky (Santacroce, 1987) and characterized by both effusive and explosive regimes (Andronico et al., 1995). The volcanic complex is located in the Campania plain (southern Italy) at the intersection of two main fault systems oriented NNW–SSE and NE–SW (Bianco et al., 1997). The last eruption, in March 1944, was effusive (Berrino et al., 1993). It may have started a new obstructed conduct phase and hence a quiescent stage.

Table 1

Station	E–W (UTM)	N–S (UTM)	Altitude (a.s.l.) (m)
BAFM	450,372	4,518,076	594
BKEM	452,677	4,518,762	850
BKNM	451,875	4,520,020	865
FTCM	452,692	4,516,337	350
OVO	449,190	4,519,705	600
POLM	447,910	4,522,499	181
SGVM	450,568	4,518,706	734

The seismic activity is actually the unique indicator of the internal dynamics (see e.g. De Natale et al., 1998). Seismicity studies are of extreme importance for the high risk volcanic area of Mt. Vesuvius. As an overall, the seismicity of Mt. Vesuvius is characterized by a mean rate of approximately 300 events per year. The largest earthquake in the area (reasonably since the last eruption – 1944 – see Del Pezzo et al., 2004) occurred in 1999, and has been associated with regional and local stress fields (Bianco et al., 1997). The main features of the earthquake space and time distribution are described in the papers by Scarpa et al. (2002), hereafter cited as SCA02, and Del Pezzo et al. (2004). In the study of SCA02 the relocated seismicity appears to extend down to 5 km below the central crater, with most of the energy (up to local magnitude 3.6) clustered in a volume spanning 2 km in depth, positioned at the border between the limestone basement and the volcanic edifice. The hypocentral locations for the data used in the present article show the same pattern of the overall seismicity (Fig. 1).

The earthquakes recorded at Mt. Vesuvius are mostly of volcano-tectonic type (VT), with fault-plane orientations, showing an highly non-regular spatial pattern. The spectral content of the P- and S-wave trains of the VT events is compatible with stress drops spanning a range between 1 and 100 bars (100 bars for the largest magnitude) and focal dimensions of the order of 100 m (Del Pezzo et al., 2004).

The velocity structure beneath Mt. Vesuvius, in the depth range from the Earth surface to 10 km, has been deduced by seismic tomography. Auger et al. (2001) suggest the presence of a melting zone at a depth of about 8 km, on the base of the TOMOVES experiment results (see the book by Capuano et al., 2003 and the numerous references therein). At smaller scale, between the topographical surface and 5 km of depth, SCA02 evidence a low velocity contrast between 1 and 2 km, possibly associated with the presence of aquifers. No shallow and small magma chambers are visible at the resolution scale reached by SCA02.

3. Data selection

In the present work we utilized a total number of 6609 waveforms, obtained from a selection of 826 earthquakes recorded from January 1996 to June 2000 at seven 3-component stations that are the analogical station OVO (66 dB dynamic range, three component) sampled at 100 s.p.s. and 6 digital, high dynamic (120 dB, gain ranging), 1 Hz, seismic stations sampled at 125 s.p.s. (Table 1). Analog anti-aliasing filter with 25 Hz cut-off frequency operated on all the data logger prior to sampling. Data selection has been made on the base of the following pre-requisites: the best signal to noise

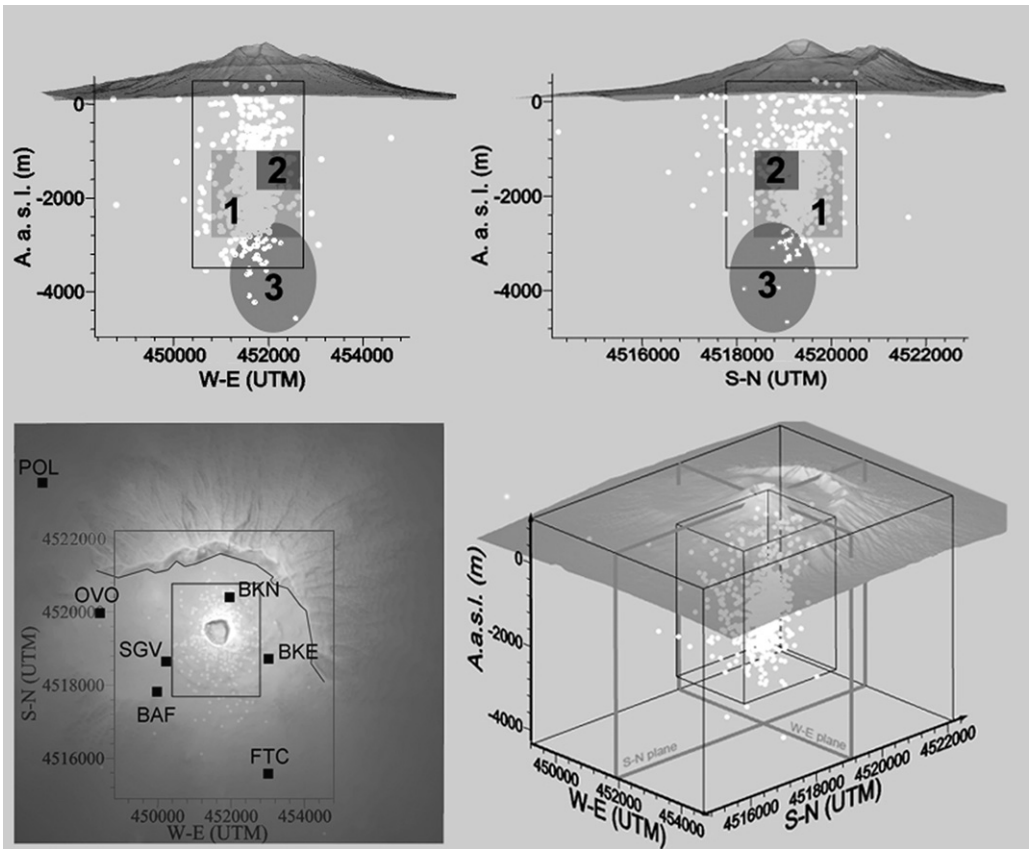

Fig. 1. Lower-left panel: Map of Mt. Vesuvius with station positions (black squares) and hypocentral locations (white dots) of the seismic events used in the present work. Black broken line depicts the old caldera rim. Upper-left and upper-right panels represent respectively the W–E and S–N sections, also reported as "W–E plane" and "S–N plane" in the lower-right "wide angle" view. The high resolution region (HRR) is roughly depicted by the inner polyhedron in the wide angle view. The solid line rectangles in the upper left, upper right and lower left panels represent the sections of the HRR. The zones marked with 1 and 2 represent the zone in which the robustness test results are reported respectively in Tables 4 and 5. The ellipsoidal zone marked with 3 shows the area with the maximum seismic energy release.

ratio, the absence of spikes and other disturbances in the waveforms, a minimum coda duration (from origin time) of 15 s and the absence of secondary events in the early coda. In doing this selection we implicitly restricted the earthquake magnitude in the range from 1.6 to 3.0, because small aftershocks are often present in the coda of larger events. Location of the 826 earthquakes (Fig. 1) was obtained using *P*-picking of all the available seismic stations constituting the monitoring network (www.ov.ingv.it) with a non linear procedure based on a grid-search algorithm (Lomax et al., 2001); ray-tracing was calculated using the 3-D velocity model obtained by SCA02.

4. Methods

4.1. Ray tracing

We used a Thurber-modified approach (Block, 1991) to trace the path of each ray in the 3-D velocity structure of Mt. Vesuvius obtained by SCA02. This is an extension of the approximate ray-bending method (Um and Thurber, 1987) that works well in velocity structures characterized by fairly sharp velocity variations, like that of Mt. Vesuvius. The only limitation is that the method does not compute reflected ray paths, that anyway are not taken into account in the present work. After dividing the whole structure to be investigated in three different grids (respectively with 1800, 900 and 300 m cubic cell size) we stored in a database the length of each ray, connecting each source to each receiver, and the length of the ray-segments crossing each cell. This database is necessary for the multiple-resolution inversion approach, as discussed later.

4.2. Single-path attenuation with the coda-normalization (CN) method

The CN method is widely used to retrieve attenuation parameters independently of the site and instrumental transfer function (Aki, 1980; Sato and Fehler, 1998). Del Pezzo et al. (2006b) used this approach for the estimation of single path total *Q*-inverse to map the *S*-wave attenuation structure in Mt. Vesuvius area, using a subdivision of the investigation volume in cubic cell of 900 m in a single-scale approach. Even though the method used to estimate the single path inverse total-*Q* has been already described and discussed in Del Pezzo et al. (2006b), we report in Appendix A a synthesis for sake of completeness.

Our reference equation (see Appendixes A and B for any detail) is

$$\frac{E_{ij}(f,r)}{E^C(f,t)} r_{ij}^2 = \frac{1}{P(f,t_c)} \exp\left[-2\pi f \int_{rij} \frac{\mathrm{d}l}{v(l) Q_T^{ij}(l)}\right] \quad (1)$$

Taking logs of both sides of Eq. (1) and approximating the line integral with a sum, we can write

$$d_k^C = \frac{1}{2\pi f} \ln\left(\frac{1}{P(f,t_c)}\right) - \sum_{b=1}^{N\_cells} l_{kb} s_b Q_b^{-1} \quad (2)$$

where d_k^C represents the log of energy spectral ratio between S and coda pre-multiplied for the squared ray-length and divided for $2\pi f$. N_cells is the total number of blocks crossed by the ray, l_{kb} is the length of the k th ray-segment intersecting the b th block characterized by slowness s_b and inverse quality factor Q_b^{-1}. In this formulation we use the suffix k to indicate the k th ray of the suite of rays connecting stations to sources. Eq. (2) can be rewritten separating Q_b^{-1} into an average $Q_b^{-1}, \langle Q_b^{-1}\rangle$, that we assume to be equal to the average quality factor for the whole area (Q_T^{-1}), and an incremental δQ_b^{-1}. It results

$$\tilde{d}_k^C = \sum_{b=1}^{N\_cells} l_{kb} s_b \delta Q_b^{-1} \tag{3}$$

where

$$\tilde{d}_k^C = \frac{1}{2\pi f} \ln\left(\frac{1}{P(f, t_c)}\right) - d_k^C - Q_T^{-1} \sum_{b=1}^{N\_cells} l_{kb} s_b \tag{4}$$

Eq. (3) represents a linear system of N_k equations in N_cells unknowns that can be inverted, as discussed in the next chapters.

4.3. The estimate of the observables with the CN method

Prior to the application of the CN method we checked the temporal stability of the S-wave time window for the radiation pattern effect, as widely described in Appendix B. Accordingly, we set the duration of the S-wave time window at 2.5 s starting from the S-wave arrival time. Coda signal time window starts at 8 s lapse time and ends at 12 s, since most of our data show a favorable signal-to-noise ratio (> 3) for lapse time smaller than 12 s. A discrete Fourier transform (DFT) is applied to the signals after windowing (we used a cosine taper window with tapering at 10% both for S and coda) for both the horizontal components of the ground motion. We calculate the S spectral amplitude averaged in the frequency bands centered at the values of frequency, f_c, reported in Table 2, with bandwidths ($\pm\Delta f$), and finally log-averaged over the components; we thus obtain the ratio between the S-wave spectrum and the coda spectrum. The natural logarithm of this ratio estimates d_k^C of formula (4). The constant in Eq. (2) has been already estimated by Del Pezzo et al. (2006b) for the area under study.

4.4. The slope-decay (SD) method

The validity of the CN method is tested using a version of the so called slope decay method, which has been widely used to estimate the attenuation coefficient in many regions of the world (Nava et al., 1999; Giampiccolo et al., 2003; Gudmundsson et al., 2004).

As well known, the amplitude spectral density for S and P waves for frequencies higher than the corner frequency can be expressed as the product of source, path and site effects as

$$A_{ij}^{HF}(f, r) = S_i^A(f) I_j(f) T_j(f) G_{ij}(r) \exp\left(-\pi f \frac{t_{ij}(r)}{Q_T^{ij}(r)}\right) \tag{5}$$

Table 2

$-\Delta f$	f_c (Hz)	$+\Delta f$
8.2	12	15.8
12.4	18	23.6

where $A^{HF}(f, r)$ is the high-frequency spectral amplitude of the P- or S-wave radiation emitted by the source i at total distance r measured along the source (i)-station (j) ray-path; f is the frequency; $S_i^A(f)$ is the amplitude spectrum at source; I_j is the instrument transfer function; T_j is the site transfer function and G is the geometrical spreading term; t_{ij} is the travel time along the ray of length r and Q_T^{ij} is the total quality factor measured along the ray-path. In the present formulation we assume that the high frequency amplitude spectrum at the source can be described by a function $S_i^A = \text{const}_i f^{-\gamma}$, γ being a constant for the whole set of data utilized. Taking the natural logarithm and making the derivative of the Eq. (5) respect to frequency, f, it can be written for each ray-path:

$$D_f(\ln A_{ij}^{HF}) = D_f(\ln S_i^A) - \pi \frac{t_{ij}(r)}{Q_T^{ij}(r)} \tag{6}$$

where D_f is the symbol of derivative. In obtaining formula (6) we assumed the independence of frequency for the site and instrument transfer function. The independence of frequency for the site term has been confirmed by Galluzzo et al. (2005) who studied the site transfer function at Mt. Vesuvius. The transfer function of the instruments is flat with frequency in the whole frequency range investigated. Transforming the couple of indexes i j in a single integer k associated with the single ray, as in the previous section, we can write

$$D_f(\ln A_k^{HF}) = D_f(\ln S_i^A) - \pi \frac{t_k(r)}{Q_T^k(r)} \tag{7}$$

Averaging the left hand quantity of the above equation over the rays considered (k index) we obtain

$$\langle D_f(\ln A_k^{HF})\rangle_k = D_f^0(\ln A^{HF}) = \left\langle D_f(\ln S_i^A) - \pi \frac{t_k(r)}{Q_T^k(r)} \right\rangle_k = D_f^0(\ln S^A) - \pi \left\langle \frac{t(r)}{Q_T(r)} \right\rangle_k \tag{8}$$

$D_f^0(\ln S^A)$ results to be the same of $D_f(\ln S_i^A)$ (the average of the source spectral derivative equals the spectral derivative for the single event), so that we can write

$$D_f(\ln A_k^{HF}) - D_f^0(\ln A^{HF}) \tilde{=} \pi \left(\left\langle \frac{t(r)}{Q_T(r)} \right\rangle_k - \frac{t_k(r)}{Q_T^k(r)} \right) \tag{9}$$

Indicating with d^D the quantity:

$$d_k^D = \frac{1}{\pi} [D_f(\ln A_k^{HF}) - D_f^0(\ln A^{HF})] \tag{10}$$

and expressing the right hand side of Eq. (9) as already done in Eq. (1) we obtain

$$d_k^D = \left\langle \frac{t(r)}{Q_T(r)} \right\rangle_k - \sum_{b=1}^{N\_cells} l_{kb} s_b Q_b^{-1} \tag{11}$$

where the index k is referred to the k th ray.

Making the same assumption that leads to formula (3), we can finally write

$$\tilde{d}_k^D = \sum_{b=1}^{N\_cells} l_{kb} s_b \delta Q_b^{-1} \tag{12}$$

where

$$\tilde{d}_k^D = \left\langle \frac{t_k}{Q_k} \right\rangle - d_k^D - Q_T^{-1} \sum_{b=1}^{N\_cells} l_{kb} s_b \tag{13}$$

The inversion schemes (3) and (12) are formally identical, apart the constant values.

4.5. The estimate of the observables with the SD method

Direct S spectral amplitudes were obtained in the frequency band centered at $f_c = 18$ Hz, with the same bandwidth used for the CN method (Table 2). The use of only this central frequency value is justified by the spectral features of the seismicity at Vesuvius like broadly discussed in Del Pezzo et al. (2006b). We applied a DFT to windowed signals of length 2.5 s starting from the direct S travel time for both W–E and S–N components of the ground motion; then we log-averaged the spectra over the components.

We applied the SD method both to direct S waves and to direct P waves. Spectral amplitude for P waves was calculated in a time window starting from the P-wave onset and ending at 0.1 s before the S-wave picking, tapering each spectrum with a 10% cosine taper function.

The derivative was carried out for both S and P log-spectra in the frequency band starting from corner frequency (around 10 Hz for the whole set of data) and ending at 23 Hz (before the cut-off frequency of the anti-alias filter that was set up at 25 Hz). The derivative was computed using MATLAB "diffnew" routine.

5. Multi-resolution inversion

The resolution of the methods depends both on the wavelength (which has to be smaller than the cell size) and on the number of rays which sample the single cell. A frequency $f_c = 12$ Hz corresponds to a wavelength of about 200 m for S waves. For P waves (examined at 18 Hz only) the corresponding wavelength is of the order of 150 m. Taking a cell size of 300 m we observe that the blocks bordering the volume of investigation are crossed by a number of rays insufficient to ensure stability in the final solution, due to the distribution of the sources, concentrated along the crater axis and not uniformly distributed in space and depth inside the volume under investigation. This is the reason why we cannot invert the whole data set using a uniform resolution of 300 m. Consequently, we seek for solutions that can represent images in cells with a non-uniform size, as other researchers do in velocity tomography (Thurber, 1987; Sambridge and Gudmundsson, 1998). In this approach, a relatively high-resolution can be obtained in a target area with a good ray coverage (this avoids linear dependence among the system equations). To perform this task we use an iterative inversion scheme (Thurber, 1987; Eberhart-Phillips, 1990), in which we employ the results obtained in a lower resolution (LRR) as input for highest resolution (HRR). Bai and Greenhalgh (2005) describe an inversion scheme of this kind, applied to velocity tomography. Our inversion scheme is different from those above cited and will be described in the following points.

(1) The observables are calculated (both for the CN method and the SD method we apply the same inversion procedure) as above described.
(2) The attenuation factor averaged over the whole volume under study, Q_T^{-1}, is estimated with the CN method. It results in a really good agreement with that estimated by the previous works in the same area (Bianco et al., 1999; Del Pezzo et al., 2006a).
(3) The problem of Eq. (3) and (12) is solved for a volume divided in cubic blocks of 1800 m side, using a positivity constraint. Then, each 1800 m side block is divided in 8 blocks of 900 m side, and the inverse quality factors thus calculated, $(Q_b^{-1})^{1800}$, are assigned to each of this cubes.
(4) The problem is solved for the 900 m cell size resolution, taking into consideration that each ray is characterized by the attenuation factor, which has been obtained by the solution of the previous step. In this way we obtain the new quantity $(\delta Q_b^{-1})^{900}$, which represents the variation from the inverse quality factor $(Q^{-1})^{1800}$ assigned to the 900 m block in the previous step. We divide as before each 900 m block in 27 blocks of 300 m side, assigning to each of them the inverse quality factor $(Q_b^{-1})^{900}$. Also for this step we use a positivity constraint on the $(Q_b^{-1})^{900}$.
(5) Finally we solve the problem for a 300 m side cell resolution, obtaining $(\delta Q_b^{-1})^{300}$.

It is noteworthy that, whereas the data vectors and the coefficient matrices need to be recalculated at each scale, the inversion problem is always formally the same and is given by Eqs. (3) and (12). The details regarding how the data vectors and coefficient matrices are upgraded at each scale are reported in Appendix C. It is also important to note that, at each step, we accept the solutions for the blocks in which the number of ray-segments, n_R, is given by

$$n_R \geq \frac{2\text{Block\_side}}{\lambda} \tag{14}$$

This empirically determined threshold would ensure, in the assumption that the directions of ray-segments are randomly distributed in each block, that each block is homogeneously sampled.

6. Robustness, stability, checkerboard and synthetic anomaly tests

6.1. Robustness

The robustness of the method is tested using a bootstrap approach, reducing randomly the number of available equations (rays). We applied this test to all the blocks at each cell size. The solutions for blocks of 1800 m side were obtained for progressive reductions of the equations used to solve the inverse problem (see Appendix C, formula (21)); at each step we measured the quantity:

$$P = \frac{Q_b(0) - Q_b(\%)}{Q_b(0)} \times 100 \tag{15}$$

where $Q_b(\%)$ is the quality factor of the block b obtained for the reduced data set, whereas $Q_b(0)$ is the solution obtained using the whole database. We repeated the inversion 100 times for each data reduction, measuring then the average percentage. We observed in most of the cases a significant increase of the percentage for a reduction of more then 40% of the data-set. The results for all the blocks of 1800 m side solved are reported in Table 3.

We repeated the same procedure for each scale, i.e. we measured the quantity P of formula (15) for all the 900 m side blocks. We obtain a significant change in the value of P and a significant reduction of the average blocks resolved, for a random extraction of more than 40% of data. For sake of synthesis we report in Table 4 the results obtained for 8 blocks contained in a single 1800-side block which resulted to be characterized by $(Q_b^{1800})^{-1} = 0.0128$; its position is shown in the upper panels of Fig. 1 using the light grey square evidenced by number 2. The results for the other 900 m side blocks solved by the inversion are similar.

Finally, we compared the variations of P calculated with Eq. (15) for all the 300 m side blocks, observing both a significant change in the value of the parameter models and a significant reduction in the average number of blocks resolved, for the random extraction of more than 20% of data. We report in Table 5 a selection of 8 blocks of 300 m contained in the singular block of 900 m side having $(Q_b^{900})^{-1} = 0.011$ (the position of the 900 m block is shown

Table 3
Robustness test—1800 m.

Block#	1	2	3	4	5	6	7	8	9	10	11	12
P^{1800}, 10%	1%	0%	0%	13%	7%	4%	0%	0.1%	0%	0%	0%	3%
P^{1800}, 20%	1%	0%	2%	29%	9%	11%	17%	1%	0%	0%	0%	3%
P^{1800}, 30%	2%	1%	3%	28%	9%	9%	50%	0.3%	0%	0%	0%	2%
P^{1800}, 40%	3%	3%	10%	29%	8%	16%	87%	2%	1%	0%	0%	8%
P^{1800}, 50%	6%	2%	11%	62%	20%	25%	87%	3%	1%	0%	0%	9%

Robustness test at the lowest resolution; the average percentage of Eq. (15) is represented for all the blocks resolved. The increasing percentage in the first column is the data reduction.

Table 4
Robustness test—900 m.

Block#	1	2	3	4	5	6	7	8
P^{900}, 10%	1%	15%	2%	1%	10%	1%	31%	1%
P^{900}, 20%	1%	13%	15%	1%	12%	8%	> 100%	1%
P^{900}, 30%	1%	21%	15%	1%	16%	9%	> 100%	1%
P^{900}, 40%	2%	53%	29%	2%	30%	7%	> 100%	2%
P^{900}, 50%	2%	58%	72%	2%	40%	11%	> 100%	2%

Robustness test at the intermediate resolution; the average percentage of Eq. (15) is represented for the 8 blocks in which the single 1800 m side block of $(Q_b^{1800})^{-1} = 0.0128$ which includes the cone was divided. The increasing percentage in the first column is the data reduction.

Table 5
Robustness test—300 m.

Block#	1	2	3	4	5	6	7	8
P^{300}, 10%	12%	16%	21%	59%	30%	5%	1%	14%
P^{300}, 20%	37%	90%	54%	99%	17%	48%	90%	70%
P^{300}, 30%	> 100%	> 100%	67%	> 100%	69%	> 100%	98%	> 100%

Robustness test at the highest resolution; the average percentage of Eq. (15) is represented for 8 blocks contained in a single 900 m side block of $(Q_b^{900})^{-1} = 0.0110$. The increasing percentage in the first column is the data reduction.

in the upper panels of Fig. 1 using the dark grey square evidenced by number 1).

6.2. Stability

The stability of the method is checked by changing the value of the constants in formulas (4) and (13). In formula (4) we let g_0 to vary between the values of $g_{min} = 1$ and $g_{max} = 2.5$ that represent the error limits of the average g as reported in Del Pezzo et al. (2006a). In formula (13) we let $\langle(t_k/Q_k)\rangle$ to vary in the interval $[-3\sigma + \langle(t_k/Q_k)\rangle, +3\sigma + \langle(t_k/Q_k)\rangle]$. The results do not change significantly. In both (4) and (13) we let Q_T^{-1} to vary in the interval $[-3\sigma + Q_T^{-1}, +3\sigma + Q_T^{-1}]$

For the resolution of 1800 m the variations of each parameter model obtained for the extreme values are reported in Table 6.

For the intermediate resolution (900 m) we repeat the same procedure setting maximum and minimum values of $(Q^{1800})^{-1}$ and Q_T^{-1} sampled in their confidence interval (3σ). The 8 blocks considered in Table 7 are the same of Table 4.

For the maximum available resolution (300 m), using the results obtained changing the values of Q_T^{-1}, $(Q_b^{1800})^{-1}$ and $(Q_b^{900})^{-1}$ in their confidence interval, we obtain the results shown in Table 8 for the 8 blocks considered in Table 5.

6.3. Checkerboard inside the HRR

Our results have been tested imposing an a priori attenuation structure to the area: we assumed an homogeneous medium in the LRR and a checkerboard distribution of the quality factors in the volume where the HRR is located, resolving only the blocks crossed by at least 5 rays per block, following Eq. (14). Using the CN method we calculated the true spectral ratios and added to these values a Gaussian random error calculated with a random number generator with zero mean and 10% sigma.

The synthetic structure results to be extremely well resolved in the central part, whereas the quality of the reproduction of the input values decreases toward the borders of the volume under investigation. The checkerboard test results (Figs. 2 and 3) are shown both for the W–E and S–N sections already shown in Fig. 1, and for five horizontal slices in the depth range between −500 and −3500 m.

In Fig. 2 it can be noticed that the input checkerboard structure (W–E and S–N sections in panel a) is well reproduced everywhere except in a small area toward N–E, corresponding to the geological structure of Mt. Somma (the same sections in panel b); this is due to the lack of seismic sensors in this area. The negative variations in the inverse quality factors under −3000 m sometimes explode, always reconstructing well the zones with low Q_S^{-1}. In Fig. 3 the five panels on the left present five horizontal sections of the volume contain-

Table 6
Stability test—1800 m.

Block#	1	2	3	4	5	6	7	8	9	12
$[(Q^{1800})^{-1}] \times 10^{-2}$	1.98	1.79	1.50	2.44	1.28	1.37	0.92	2.86	0.51	3.16
$[(Q^{1800})^{-1}] \times 10^{-2}, (Q_T^{min})^{-1}$	1.83	1.67	1.72	1.84	1.28	1.43	1.15	2.72	0.49	3.21
$[(Q^{1800})^{-1}] \times 10^{-2}, (Q_T^{max})^{-1}$	1.88	1.69	1.10	2.88	1.11	1.08	0.54	2.74	0.40	2.81

Stability test at the lowest resolution; the value of the inverse quality factor of each resolved block is dependent on the maximum ($(Q_T^{max})^{-1} = 0.026$) and minimum ($(Q_T^{min})^{-1} = 0.008$) average inverse quality factor allowed.

Table 7
Stability test—900 m.

Block#	1	2	3	4	5	6	7	8
$[(Q^{900})^{-1}] \times 10^{-2}$	1.79	0.52	0.96	1.79	2.75	1.64	0	1.79
$[(Q^{900})^{-1}] \times 10^{-2}, (Q_T^{min})^{-1}, (Q_{bmin}^{1800})^{-1}$	1.88	0.46	1.12	1.88	2.36	1.77	0	1.88
$[(Q^{900})^{-1}] \times 10^{-2}, (Q_T^{max})^{-1}, (Q_{bmax}^{1800})^{-1}$	1.67	0.58	0.80	1.67	3.14	1.51	0	1.67

Stability test at the intermediate resolution; the value of each inverse quality factor is both dependent on the maximum ($(Q_T^{max})^{-1} = 0.026$) and minimum ($(Q_T^{min})^{-1} = 0.008$) average inverse quality factor and the maximum ($(Q_{bmax}^{1800})^{-1} = 0.0188$) and minimum ($(Q_{bmin}^{1800})^{-1} = 0.0167$) inverse quality factor of the block in which they are contained.

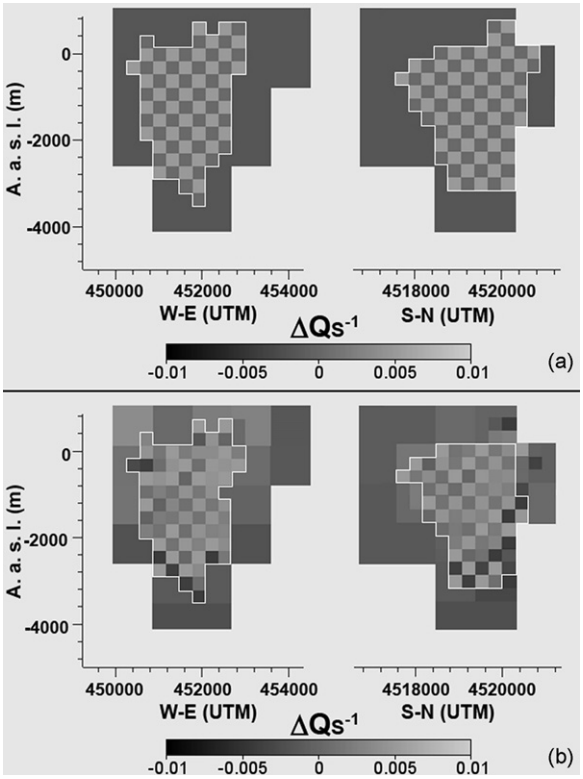

Fig. 2. Checkerboard test in the HRR. (a) Input. W–E and S–N sections (also marked in Fig. 1, lower right panel); the white lines include all the maximum resolution cells defined by formula (14). In this volume we assumed a checkerboard structure, with high Q-contrast among the blocks; a uniform attenuation medium is assumed outside HRR. (b) Output. Test results for a 10% error on synthetic data. The zones marked by the white broken lines include the cells where the checkerboard structure is effectively reproduced. ΔQ_S^{-1} grey scales represent the variation from the average quality factor.

ing the input checkerboard structure, imaging the HRR (see also Fig. 1, downward left panel); the good resolution achievable by the method used is evident in the volume constrained between 0 and −2700 m (right panels of the same figure). At $Z = -3500$ m, the volume resolved at the maximum resolution heavily decreases. Both in Figs. 2 and 3 we marked with a white broken line the effective HRR obtained using this test.

6.4. Synthetic anomaly

Following Schurr et al. (2003) we performed a second test using synthetic data by tracing rays through the real 3-D V_S model, trying to check the effective availability of the results which will be discussed in the following chapter. This test presents a Q_S^{-1} model created using anomalies comparable in size to those observed using the real data-set (W–E and S–N sections in Fig. 4, panel a) but with slightly different geometries. A 10% normally distributed error was applied to the spectral ratios. The test shows that the anomalies are generally well recovered between the surface and −3000 m (W–E and S–N sections in Fig. 4, panel b), even if their dimensions are comparable with the maximum resolution achievable. In the depth range between −3000 and −4500 m the reproduction of Q_S^{-1} anomalies of the order of maximum resolution is more difficult; that results are consistent with the ones of the checkerboard test (Fig. 3, $Z = -3500$ m); however we will be able to treat this region at a resolution of 900 m thanks to our new data-set.

7. Results

Using the present multi-resolution method, we obtained the attenuation structure under Mt. Vesuvius in two frequency bands (Table 2), respectively centered at 12 and 18 Hz. The images have a resolution of 300 m in the sub-volumes with a higher ray coverage marked in Figs. 2 and 3 with a white broken line. All the results obtained are shown in Figs. 5–7. All the depths (negative downward), are calculated respect to the sea level. In Figs. 6 and 7 the images relative to the velocity tomography (SCA02) are also shown. The present database is a subset of the database used in the velocity tomography.

In Fig. 5 the results of S-wave attenuation imaging obtained with both CN and SD are reported for sake of comparison.

Using CN technique, an estimate of the variation of the S-wave inverse total-Q respect to their mean was obtained for the two frequency bands (12 and 18 Hz), where the signal to noise ratio value resulted sufficiently high for this analysis (see Del Pezzo et al., 2006b). These images are reproduced in panels a and b of Fig. 5. Using SD technique a unique image at 18 Hz was obtained (panel c).

Figures shown in panels a and b are very similar except for an higher attenuation zone (turquoise) located in a depth range between −2500 and −3500 m centered at 452,000 onto the W–E section, visible in panel b.

Table 8
Stability test—300 m.

Block#	1	2	3	4	5	6	7	8
$[(Q^{300})^{-1}] \times 10^{-2}$	5.61	1.78	1.91	0.39	1.44	0	2.26	0
$[(Q^{300})^{-1}] \times 10^{-2}, (Q_{Tmin})^{-1}, (Q_{bmin}^{1800})^{-1}, (Q_{bmin}^{900})^{-1}$	2.59	1.76	1.34	0.05	1.29	0	2.60	0
$[(Q^{300})^{-1}] \times 10^{-2}, (Q_{Tmax})^{-1}, (Q_{bmax}^{1800})^{-1}, (Q_{bmin}^{900})^{-1}$	6.91	1.99	2.01	1.59	1.32	0	1.34	0

Stability test at the highest resolution; the value of each inverse quality factor is both dependent on the maximum ($(Q_T^{max})^{-1} = 0.026$) and minimum ($(Q_T^{min})^{-1} = 0.008$) average inverse quality factor. It is also dependent on the maximum ($(Q_{bmax}^{1800})^{-1} = 0.0188$, $(Q_{bmax}^{900})^{-1} = 0.0177$) and minimum ($(Q_{bmin}^{1800})^{-1} = 0.0167$, $(Q_{bmin}^{900})^{-1} = 0.0151$) inverse quality factor of the blocks in which they are contained.

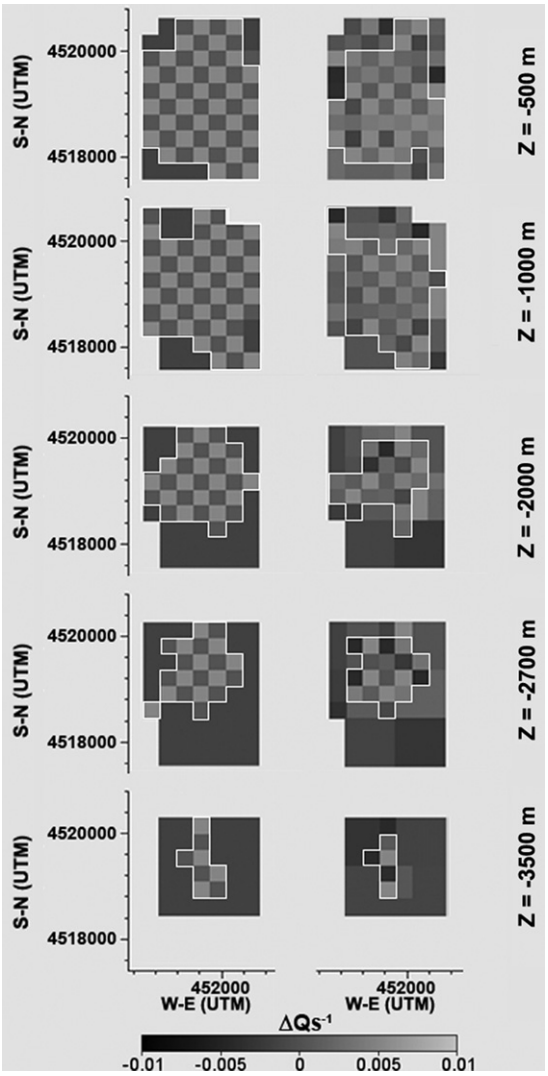

Fig. 3. Left hand panels. Five horizontal slices at different depths (Z value respect to the sea level) of the volume containing the HRR. The white lines include all the maximum resolution cells defined by formula (14). The sections represent the input checkerboard structure also described in Fig. 3, with the same colorscale. Right hand panels. The figures represent the test output; the zones marked by the white broken lines include the cells where the checkerboard structure is effectively reproduced; the zones marked by the white broken lines include the cells where the checkerboard structure is effectively reproduced.

Comparing panels (b) and (c), we notice that in the HRR the images are similar. Outside the HRR slight differences between the two images appear in the W–E section, at a depth of 1000 m between coordinates 453,000 and 454,000. In this region CN method (panel b) gives a high attenuation contrast zone whereas the contrary occurs for SD method (panel c). The SD method produces in general a less uniform image respect to the CN method.

Fig. 6, panel (a) reports the W–E and S–N sections of the S-wave attenuation images at 18 Hz (hereafter we will always refer to the CN method); in the same figure the S-wave velocity (panel b), P-wave attenuation (panel c) and P-wave velocity (panel d) for the W–E and S–N sections are also represented. V_P/V_S ratio as a function of depth (calculated as an average over the slices at different depth) is superimposed to all the figures. The color scale in panels (a) and (c) represents the variation of the inverse quality factor respect to the mean S- or P-wave attenuation; the color scale of panels (b) and (d) represents the absolute S- and P-wave velocity.

Fig. 7 represents five image slices at the depths −500, −1000, −2000, −2700 and −3500 m. Color scales represent the differences respect to the average S-wave velocity (first column), S-wave attenuation (second column), P-wave velocity (third column) and P-wave attenuation (fourth column) calculated for each slice. This quantities follow the behavior of the absolute P- and S-waves velocities and attenuations (in the discussion we will not make any difference between the absolute quantity and the variation respect to the mean), but they highlight more properly the lateral variation of this quantities.

8. Discussion

The HRR is localized essentially under the central part of the cone till to a depth of 3.5 km (see Figs. 2 and 3). In this zone we have thus an S-wave attenuation image with a resolution improved respect to that obtained by Del Pezzo et al. (2006b) using a single scale approach. Laterally, the resolution becomes lower due to the station density, which is not comparable with the cell dimension (for a wider discussion on station density and resolution see Bai and Greenhalgh, 2005).

8.1. Frequency dependence of the S-wave attenuation

Results described in (Del Pezzo et al., 2006b) were confirmed; the results obtained using the present multi scale approach show better resolved images. In general, the 3-D attenuation pattern shows a Q which clearly increases with depth in the 12 and 18 Hz frequency band(Fig. 5, panels a and b), showing clearly visible attenuation contrasts localized along the borders of already known structures (see e.g. SCA02) like the carbonate basement, well visible at the maximum resolution in the Q_S^{-1}, Q_P^{-1}, V_S and V_p images at −1500 m (see Fig. 6, all panels). In the HRR the independence of attenuation from frequency is confirmed in the frequency range between 12 and 18 Hz. Looking carefully at the (a) and (b) panels of Fig. 5 it is noteworthy the relative contrast localized approximately east of the central cone between −2500 and −3000 m. The synthetic test shown in Fig. 4 clearly represent the damping of low variation in δQ^{-1} at the maximum resolution in this depth range, but the anomaly has clearly a size bigger than 300 m. This contrast is not evident in panel (b) for the 12 Hz image, and this is possibly due to the different linear dimensions of the anomalous region sampled by the different wavelength.

8.2. Comparison between CN and SD images

The results obtained in the present paper with the SD method are intriguing, as they add new information about the volcano structure at small scale. Moreover, SD method allowed to obtain a P-wave attenuation structure (in the band centered at 18 Hz) to be compared with that obtained for S-waves.

Under the cone the images obtained at 18 Hz respectively with CN and SD method for S-waves are similar, showing clearly the same dependency of δQ^{-1} with depth (Fig. 5, panel b and c). In general the CN images appear much more smoothed than the SD ones. In the HRR most of the attenuation contrasts follow the same pattern, being sometimes different in value.

The sole significant differences between CN and SD images can be observed between the depths of 1000 and 2000 m in the N–E quadrant (corresponding at surface with the geological structure of Mt. Somma). In this volume (Fig. 5 panels b and c) the interface between carbonate basement and the overlying volcano materials, is not clearly defined in the SD image. On the other hand, this interface is clearly evidenced by SD method applied to P-waves, and very

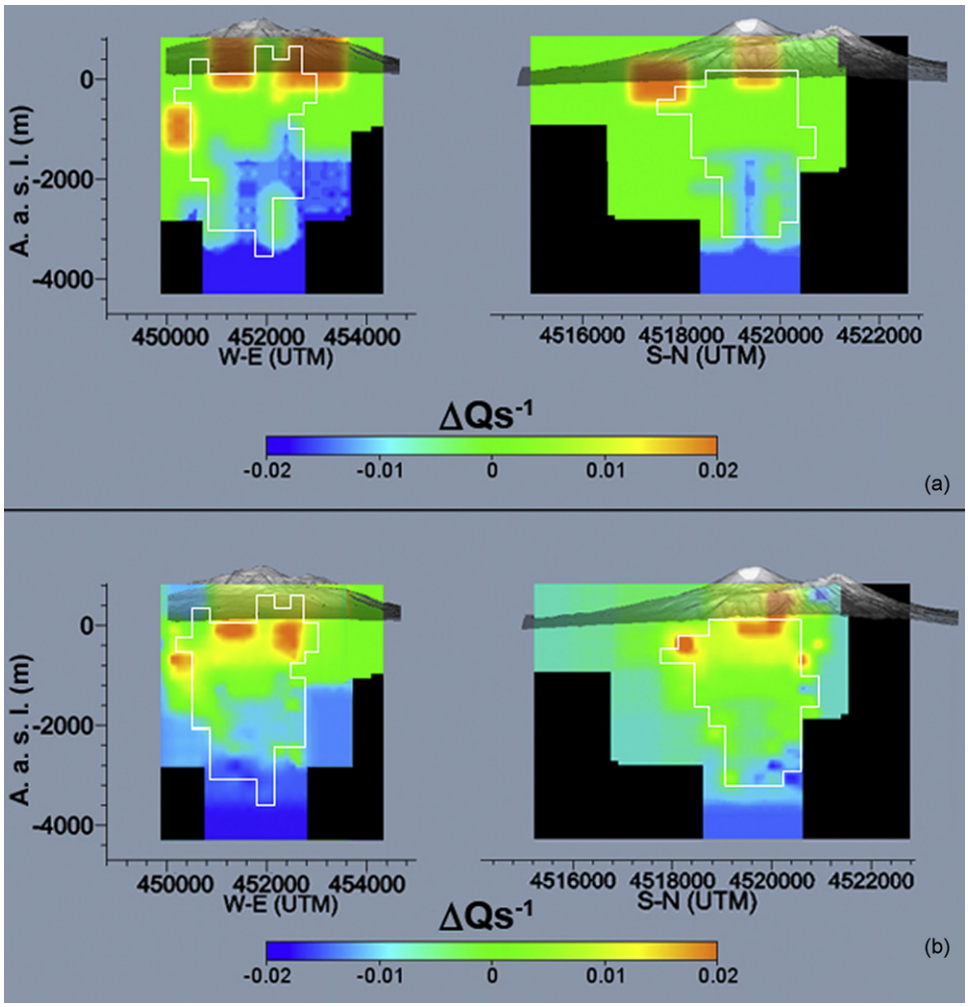

Fig. 4. Synthetic anomaly test. The input structures (panel a) are included in a volume characterized by uniform attenuation. The output (panel b) show the reconstruction of the anomalies. Black areas are not resolved in the inversion. Colorscales refer to the variations respect to the mean inverse quality factor. The zones marked by the white broken lines include the cells where the checkerboard structure is effectively reproduced.

well defined by the velocity tomography (Scarpa et al., 2002; Zollo et al., 2002).

The discrepancy above discussed may be due to the presence of a non-uniform scattering wave field Wegler (2003) that may produce a bias in the normalization of *S*-spectrum with coda spectrum. Despite this problem, the independence of CN of site transfer function makes CN approach particularly suitable for the application to volcanic areas, where site effects may severely affect the spectrum of *S*-radiation emitted by the VT earthquakes.

8.3. Joint interpretation of velocity and attenuation images

8.3.1. General pattern

We first analyzed the velocity images, isolating the volumes characterized by strong laterally and/or in depth contrasts, velocity inversions, variations from the average V_P/V_S. Then, we associated them with the corresponding volumes in all the other available images. Comparing V_P with Q_P^{-1} and V_S with Q_S^{-1} images (Fig. 6, all panels) we observe that in general high V_P zones correspond to low Q_P^{-1} volumes and that high V_S zones correspond to low Q_S^{-1} volumes; the unique evident exception is the volume located under the central cone,confined in the depth range between −1000 and −2000 m, where the pattern is characterized by a low V_S and V_P corresponding to high variation in attenuation (Q_S^{-1} and Q_P^{-1} strongly increase with depth).

8.3.2. The shallower structures

In average, the attenuation of the *S*- and *P*-waves increases toward North and East in all the images for the volumes above the sea level (Fig. 6, panels a and c); interestingly, the S–N section of the Q_S^{-1} image (panel a) shows a low attenuation inclusion (green surrounded by orange, not included in the HRR) of the order of a 900 m block, corresponding with the structure of Mt. Somma. This mountain surrounds the central cone in the North and East quadrants (Fig. 1, down left) and is characterized by higher rigidity older age lavas.

In the HRR (marked with a broken white line in Fig. 2, panel b), velocity and attenuation images clearly evidence the presence of a contrast between the volcanic structure and the volume underneath at 0 m; this contrast marks the first interaction between the recent products of the volcano activity and the older higher rigidity materials.

In Fig. 7 ($Z = -500$ m) it is evident that a low attenuation zone (roughly surrounded by the rectangle 1) is strongly correlated with an high V_S and V_p zone in the same position. This area is located inside the HRR (see Fig. 3, panel a) and may represent the residual lava emitted during the last eruptions, completely solidified in the present time.

In the same slice (Fig. 7, $Z = -500$) we observe that the western part is characterized by low Q_S^{-1}, high Q_P^{-1} and low V_P/V_S. This features, in particular the opposite pattern of Q_S^{-1} and Q_P^{-1}, may

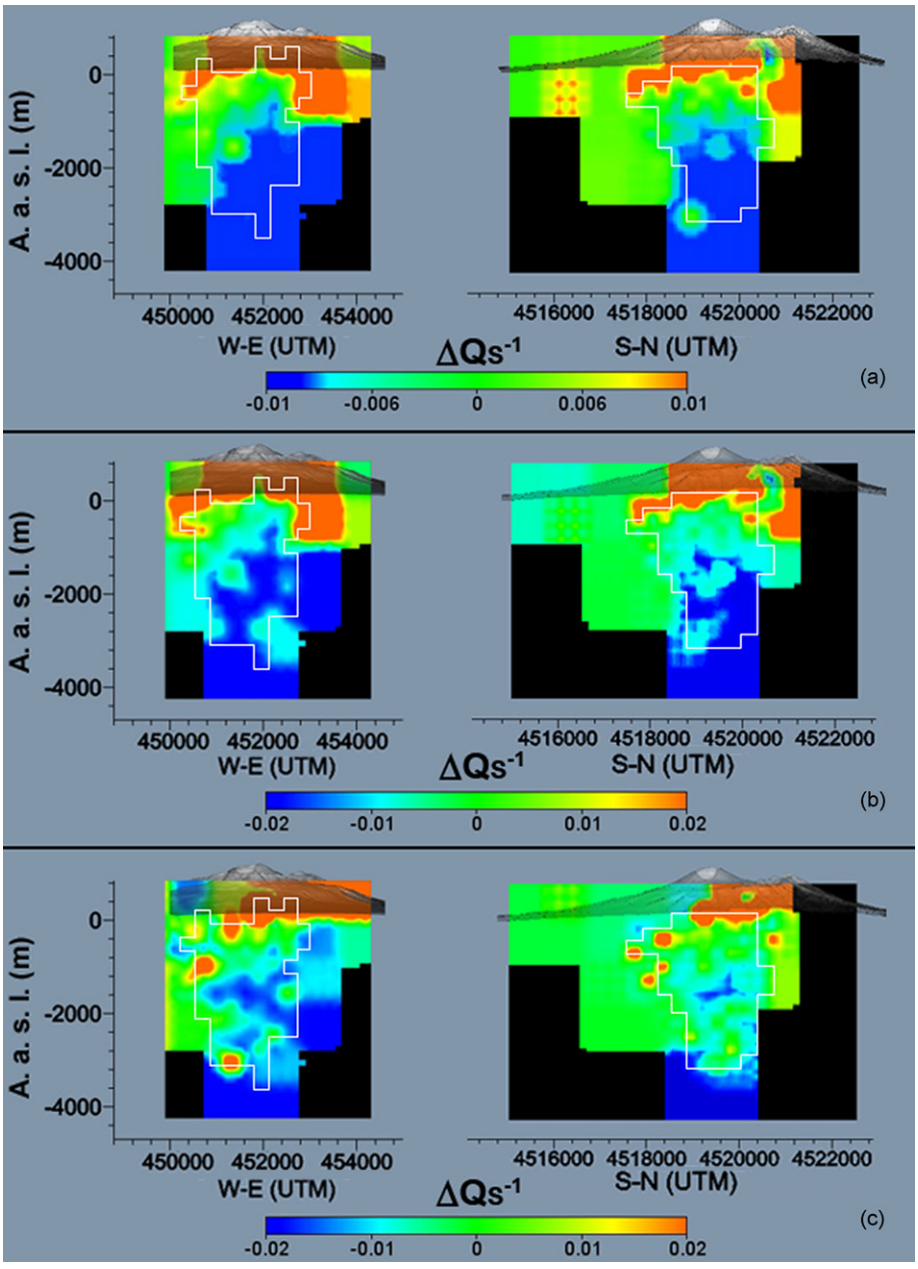

Fig. 5. Results of the attenuation tomography inversion, in the frequency band centered at 12 Hz (panel a), and 18 Hz (panel b) for the CN method, compared with the results obtained at 18 Hz for the SD method (panel c). W–E and S–N sections are those marked in Fig. 1(downright panel). Black areas are not resolved in the inversion. Colorscales refer to the variations respect to the mean inverse quality factor. The zones marked by the white broken lines include the cells where the checkerboard structure is effectively reproduced.

be compatible with the presence of a CO_2 reservoir (Hansen et al., 2004). This interpretation is corroborated by the presence of the above discussed low attenuating body in the central part of the figure. As reported by Hansen et al. (2004), when the magma rises, the decrease in confining pressure causes the magma to decompress and the biggest part of CO_2exsolves; however, when the magma cools, a modest amount of CO_2 can be definitely trapped in the rock matrix, and could explain the observed low V_P and low V_P/V_S anomalies. This interpretation is confirmed by the laboratory experiments of (Ito et al., 1979; Spencer, 1979; Sengupta and Rendleman, 1989). Summarizing the results from these papers, at pressure below the saturation pressure (as should be at a depth of −500 m), the presence of gas can lead to a decrease in V_S and V_P, an increase of Q_S^{-1}, and an anomalous decrease of Q_P^{-1}, the same results obtained in our work.

The presence of melt or partially melt rocks would lead to a low V_P, a low V_S, high V_P/V_S ratio, high Q_P^{-1} and high Q_S^{-1}. In the depth range around −500 m there is consequently no evidence supporting the presence of patches of magma with dimensions larger than cell size.

8.3.3. *The intermediate structure*

In the slices of Fig. 7 ($Z = -1000$) a zone of strong lateral contrast is evident in both the V_P and V_S images [the zone surrounded by the white line marked by number 2]. In this same zone there is no correspondence of the increasing velocity with decreasing attenuation, as already discussed in the "General pattern" section. The low

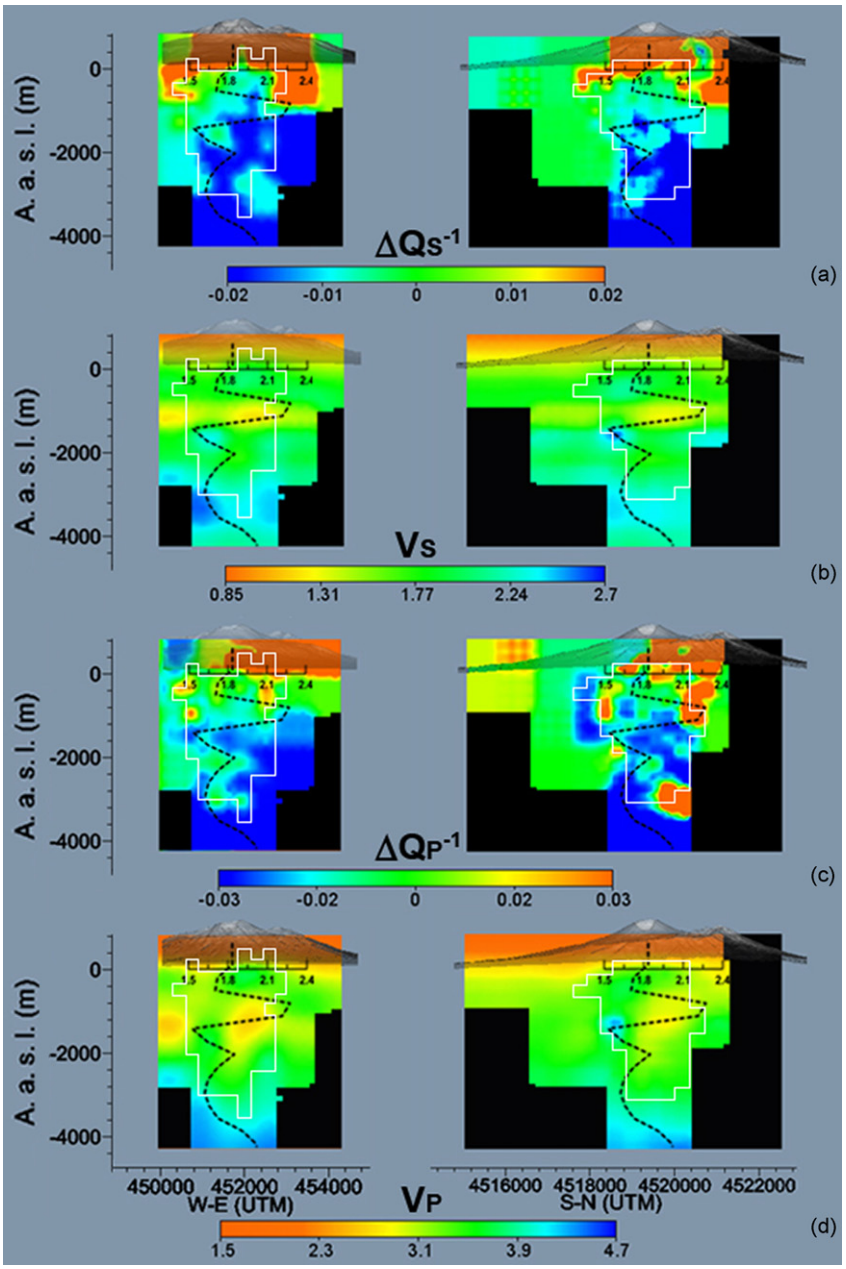

Fig. 6. The W–E and S–N sections represent the attenuation structure inferred for *S*-waves (CN method), in the frequency band centered at 18 Hz (panel a), and the *S*-velocity structures inferred by Scarpa et al. (2002) (panel b). The dashed line represents the V_P/V_S pattern with depth and is drawn on all panels. The *P*-wave attenuation (SD method, 18 Hz) and velocity (inferred by Scarpa et al., 2002) are also represented in panels c and d. The colorscales in panels a and c refer to the variations respect to the mean inverse quality factor obtained in the inversions for *S*- and *P*-waves. The colorscales in panels b and d represent the absolute *S*- and *P*-wave velocity. Black areas are not resolved in the inversion. The zones marked by the white broken lines include the cells where the checkerboard structure is effectively reproduced.

attenuation area marked by the white rectangle 1 in Fig. 7 ($Z = -1000$m) corresponds instead to an high velocity area. This area is a section of the anomalously high-velocity volume (Fig. 6, panels b and d) which seems to intrude from depth, in agreement with the interpretation reported in several velocity tomography studies (Zollo et al., 2002; Tondi and De Franco, 2003; De Natale et al., 2005, SCA02), and interpreted as related to the residual part of solidified lava from the last eruption. This high attenuation and velocity area is linked to the area marked by line 1 in Fig. 7, $Z = -500$ m.

To refine the interpretation in the depth range around −1000 m, especially for the area marked by rectangle 2 in Fig. 7, we focus the attention on the W–E and S–N sections in Fig. 6[all panels]. The zone corresponding in depth with the maximum value of the V_P/V_S ratio roughly corresponds to the interface between high attenuation and low attenuation. This interface is also characterized by low V_P and low V_S. All these observations may be interpreted as due to the presence of a fractured medium permeated by fluids, as discussed in Hansen et al. (2004) and Eberhart-Phillips et al. (2005). This interpretation should exclude the presence of a shallow patch of magma in this depth range, in the limit of our spatial resolution: in fact, our attenuation images do not show any particular evidence of melt, that, if present, should have produced both high Q_P^{-1} and high Q_S^{-1}. This results are in agreement with previous interpretation of the velocity tomography done by SCA02, and also corroborated by geochemical studies, that recognized the location of an hot aquifer

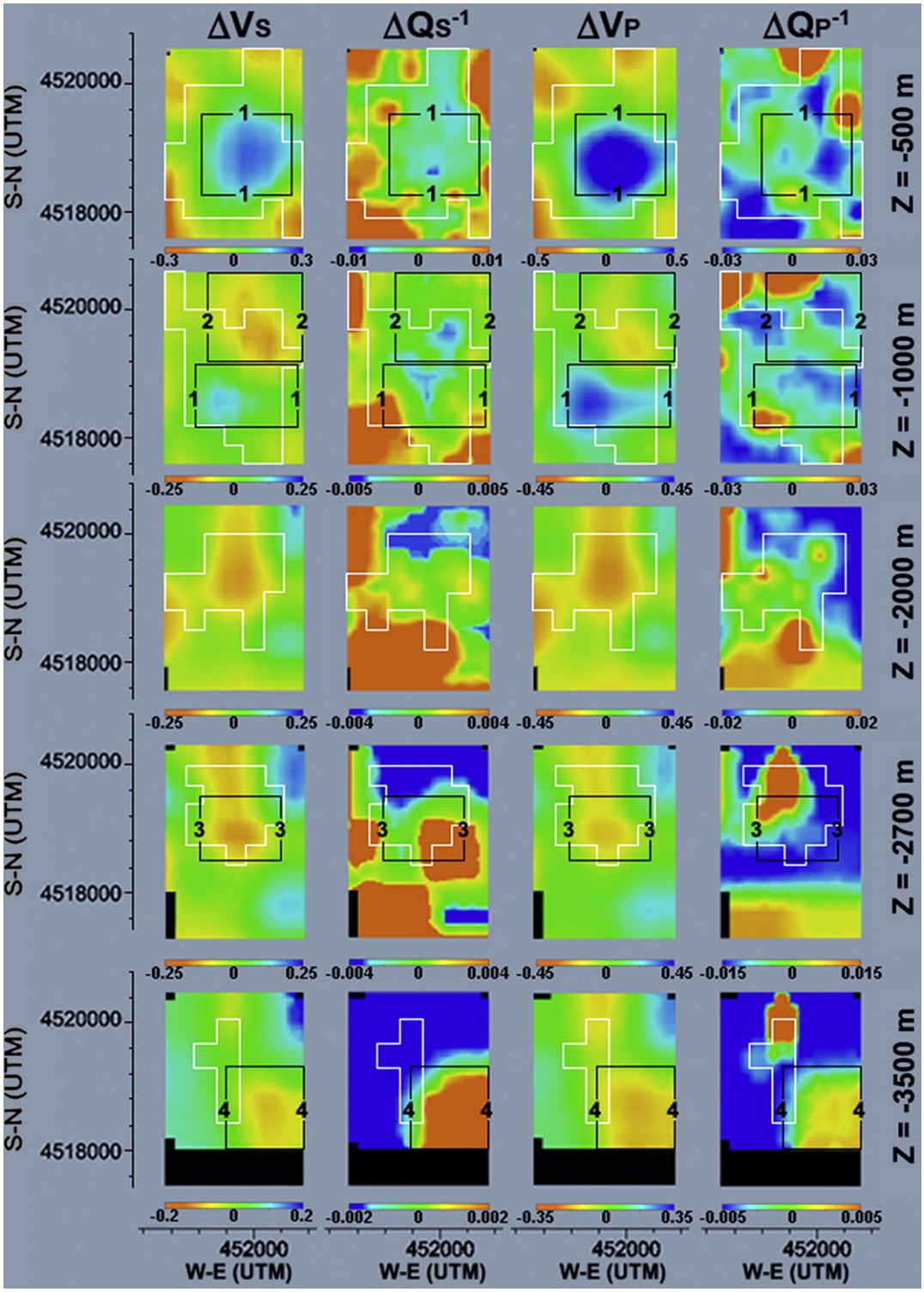

Fig. 7. Five horizontal slices of the volume containing the HRR at different depths (Z). The colorscales for S- (first column) and P-wave (third column) attenuation images represent the variations from the mean inverse quality factor calculated on each horizontal slice at each depth. The colorscales represented in the second and fourth columns respectively represent the variations of S- and P-wave velocity from the average velocity calculated at each depth. On each image we marked with numbered white rectangles zones characterized by important properties, widely discussed in the text. The zones marked by the white broken lines include the cells where the checkerboard structure is effectively reproduced.

under the cone located and modeled just in the same position, until a depth of −2200 m (Marianelli et al., 1999; Chiodini et al., 2001). The properties observed at $Z = -1000$ m can be observed also at $Z = -2000$ m (see Fig. 7). In particular a secondary maximum in V_P/V_S ratio can be observed at −2000 m. The vertical sections of Q_p^{-1} and Q_s^{-1} (Fig. 6 panels a and c) indicate the presence of lower attenuation zones around −2000 m included in a low attenuation body. This pattern can be interpreted as an highly cracked medium filled by fluids, as also evidenced by geochemical studies (Chiodini et al., 2001).

8.3.4. The deepest structure

The V_P, V_S and V_P/V_S patterns between −2500 and −4000 m (Fig. 6, panels b and d) are more regular. The $Z = -2700$ and $Z = -3500$ slices of Fig. 7 help in better understanding the velocity and attenuation features. The pattern of Q_P^{-1} and Q_S^{-1} results similar at $Z = -2700$ (Fig. 7), both in the HRR and in the LRR (see Fig. 3 at the same depths). Focusing our attention on the central part of the attenuation images (rectangle 3), we observe high contrast in both Q_S^{-1} and Q_P^{-1}, not perfectly matching the contrast in both V_P and V_S. Looking at the resolution map on this slice (Fig. 3, $Z = -2700$ m) this is not due to the lack of information achievable at the maximum resolution, but more probably to the lack of resolution at the intermediate resolution (900 m).

At $Z = -3500$ m, the decreasing attenuation corresponds to the increasing velocity outside rectangle 4, for both *P* and *S* waves. A low velocity and attenuation zone corresponding to the South-East sector of Fig. 7 at $Z = -3500$ m is clearly visible, and marked with the rectangle 4. In this region the low V_P/V_S ratio excludes the presence of partially melt rocks or fluid inclusions, suggesting on the contrary the presence of a cracked volume. This zone is spatially coincident with the zone of maximum seismic energy release, as shown in Fig. 1(upper-left and upper-right panels, the grey ellipsoidal line marked by number 3).

9. Conclusions

The present paper complements a previous preliminary study of the same area, which was carried out in a smaller volume respect to that used in the present study. The present paper uses a multi-resolution approach, which solves a 300 m cell size in the volume beneath the central crater located in the depth range between approximately 0 (the sea level) and −3500 m. The new study is based on an improved data set respect to the first one (the waveforms are more than doubled), improving both stability and robustness. The improved resolution allowed a better definition of the 3-D pattern of both Q_P^{-1} and Q_S^{-1}, thus improving the joint interpretation of previous velocity images with the present attenuation structure. The essential results show that no magma patches with dimensions larger than the cell size are visible in the images and confirm the presence of shallow hydrothermal reservoirs (between −700 and −2300 m) evidenced by geochemical studies. The high resolution achievable between 0 and −1500 m allowed a small scale imaging of the residual solidified lava emitted during the last eruptions, leading to the interpretation in terms of large patches of gas located in the first kilometer below sea level. Interestingly, the zone of maximum seismic energy release, imaged for the first time at a resolution of 900 m, coincides with a high attenuation and low velocity anomaly, easily interpretable as due to the presence of a cracked zone inside the limestone layer. These results are expected to add important constraints for the numerical models that will be adopted to simulate the next eruption, and consequently to be used for civil defense purposes.

Acknowledgements

This work is financed by INGV-DPC (Dipartimento di protezione Civile Italiana) project V3_4 and project European Union VOLUME FP6-2004-GLOBAL-3. Routine analysis has been carried out in LAV (Laboratorio di Analisi aVanzate of INGV-Naples) by Simona Petrosino and Paola Cusano, who are gratefully acknowledged. Lucia Zaccarelli greatly improved the work with numerous discussions.

Appendix A

A.1. Coda normalization method

As well known, the *S*-wave seismic energy density spectrum decays as a function of lapse-time as

$$E_{ij}(f,r) = S_i(f)\theta_{ij}(\vartheta,\phi)I_j(f)T_j(f)\frac{1}{r_{ij}^2}\exp\left(-2\pi f\frac{t_{ij}(r)}{Q_T^{ij}(r)}\right) \quad (16)$$

where $E(f,r)$ is the energy density spectrum of the *S*-wave radiation emitted by the source i at total distance r measured along the ray-path connecting source (i) and station (j); f is the frequency. $S_i(f)$ is the energy spectrum at source, modulated by the radiation pattern function $\theta(\vartheta,\phi)$. I_j is the instrument transfer function and T_j is the site transfer function. t_{ij} is the travel time along the ray whose length is r_{ij} and Q_T^{ij} is the total quality factor measured along the ray-path.

The coda energy spectrum evaluated around a given lapse time, t_c, can be considered as a function of the "average" medium properties and expressed as in Sato and Fehler (1998):

$$E^C(f,t) = S_i(f)I_j(f)T_j(f)P(f,t_c) \quad (17)$$

where $P(f,t_c)$, is independent on both source-receiver distance and directional azimuth and depends only by the earth medium. The radiation pattern term $\theta_{ij}(\vartheta,\phi)$ disappears due to the well known property of natural space averaging of coda waves (Aki, 1980). For sake of simplicity, we assume the validity of the single scattering model, but in principle equation (17) is independent of any scattering model. Dividing Eq. (16) for Eq. (17) for each source-station pair, at lapse time t_c, we obtain

$$\frac{E_{ij}(f,r)}{E^C(f,t)}r_{ij}^2 = \frac{\theta_{ij}(\vartheta,\phi)}{P(f,t_c)}\exp\left[-2\pi f\int_{rij}\frac{\mathrm{d}l}{v(l)Q_T^{ij}(l)}\right] \quad (18)$$

The spectral ratio at the left side of formula (18) is independent of energy level at source, site and instrument transfer function. In Eq. (18) the attenuation operator has been substituted with the path integral along the seismic ray, where $v(l)$ is the velocity along the path l. $\theta_{ij}(\vartheta,\phi)$ in principle depends on source azimuth ϕ and incidence angle ϑ. For a complete review of the method see Del Pezzo et al. (2006b). In Appendix B we test the independence of the spectral ratio of formula (18) of radiation pattern for ratios evaluated on signal time windows longer than 2.5 s. In this case $\theta_{ij}(\vartheta,\phi)$ can be set equal to unity.

Appendix B

B.1. Test for the independence of radiation pattern

Using the properties of the early-coda, Gusev and Abubakirov (1999) developed an empirical method to test the independence of *S*-wave spectra from radiation-pattern, when the spectrum is estimated in a time window of duration much greater than the source duration. We make a similar test for the spectral ratio between *S* and coda energy spectra calculated for the earthquakes of Mt. Vesuvius. We consider for each ray connecting the source to the receiver, the quantity:

$$A = \frac{LR}{M} \quad (19)$$

where L is the ray length, R is the spectral ratio between energies of formula (18) and $M = \exp(-\pi fr/VQ_{\mathrm{mean}})$, with V indicating the average *S*-wave velocity, is the average anelastic attenuation in the area. A is implicitly dependent only on the radiation pattern, R being

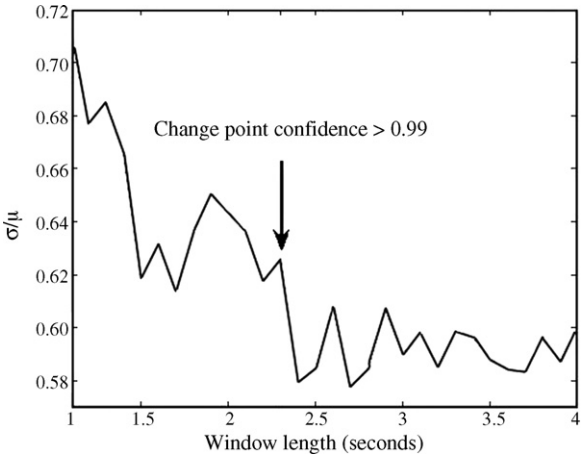

Fig. B1. The percent standard deviation, σ/μ, as a function of the window duration for an earthquake recorded at all the stations. σ/μ is obtained calculating the average, μ (over stations), of the log of spectral ratio between direct *S* radiation and coda radiation, after correcting the amplitudes for geometrical spreading and for the average *Q*. Downward arrow indicates the change-point as discussed in the text.

independent of site and instrument effects. The percent standard deviation ($\sigma_A/\langle A\rangle$) calculated averaging *A* over the stations for a single earthquake, is plotted for different time window durations in Fig. B1; this quantity abruptly decreases with increasing duration of the time window, as expected. We applied a statistical test (the "change point" test of Mulargia and Tinti, 1985) to estimate the "change point" of the pattern of *A* respect to the duration of the time window in which is calculated. The pattern results to be steady after 2.5 s at 99% confidence. Consequently, the radiation-pattern effects become negligible for time windows with a duration greater than 2.5 s. We interpret this result as due to the natural processes of averaging the radiation pattern effects that takes place in a ray-tube centered along the ray-path. The forward scattered radiation that arrives at the receiver soon after the ballistic (direct) arrival is contained inside this ray-tube (Gusev and Abubakirov, 1999). For the above reasons we assume that $\theta_{ij}(\vartheta,\phi)$ of Eq. 18 is identically equal to unity.

Appendix C

In this Appendix we explain the details relative to the points listed between 2 and 5 in Section 5.

C.1. Point 2: estimate of the average inverse quality factor (AQF)

S-waves AQF is calculated using the coda normalization method applied to the whole data-set; the Eq. (2) becomes

$$d_k^C = \frac{1}{2\pi f}\ln\left(\frac{1}{P(f,t_c)}\right) - \sum_{b=1}^{N\_cells} l_{kb}s_b[Q_T^{-1}]^C \tag{20}$$

We obtained the inverse AQF for *S* waves (Q_T^{-1}):

$$(Q_T^{-1})^{12} = 0.010 \pm 0.003$$
$$(Q_T^{-1})^{18} = 0.019 \pm 0.003$$

where the above index is referred to the center frequency.

Uncertainty is estimated assuming that each spectrum is affected by a 10% of error due to the noise. This result is in good agreement with previous *Q*-estimate for *S* waves in the area (Del Pezzo et al., 2006a).

P-waves AQF has been already calculated by Bianco et al. (1999).

C.2. Point 3: cell dimension of 1800 m

The inversion problem of Eqs. (3) and (12) is solved for a grid of 1800 m step. We can rewrite the equation as

$$\tilde{d}_k^{C,D} = \sum_{b=1}^{N\_cells\_1800} G_{kb}^{1800}[(\delta Q_b^{1800})^{-1}]^{C,D} \tag{21}$$

where the superscript 1800 stands for the step of the grid, while the superscript *C*, *D* takes into account the different methods used. The elements of the inversion matrix, G_{kb}^{1800}, are the length of the *k* th ray segment in the 1800-m side *b* th block, l_{kb}^{1800}, multiplied for his slowness s_b^{1800}:

$$G_{kb}^{1800} = l_{kb}^{1800}s_b^{1800} \tag{22}$$

Applying Eq. (14), we consider only blocks crossed by at least $n_R =$ 35rays. The problem is solved separately for each frequency band. We solve the problem using the least squares algorithm "lsqlin" deployed in MATLAB.

The percentage reduction of the residuals, computed using the formula in Gubbins (2004), results to be 65%. The inverse quality factor of each 1800 m block *b* is given by

$$(Q_b^{1800})^{-1} = Q_T^{-1} + (\delta Q_b^{1800})^{-1} \tag{23}$$

C.3. Point 4: cell dimension of 900 m

The data vector obtained solving the inversion schemes of Eqs. (4) and (13) can be updated with the solutions obtained in the previous steps. Each ray crosses a medium whose quality factor is no more Q_T, and is affected by the quality factors of the cube that it effectively crosses. The elements of the data vector must represent the effect of the attenuation structure obtained in the previous steps. They become respectively:

$$(\tilde{d}_k^C)^{1800} = \left\langle \frac{1}{2\pi f}\ln\left(\frac{1}{P(f,t_c)}\right)\right\rangle - d_k^C - Q_T^{-1}\sum_{b=1}^{N\_cells\_900} l_{kb}^{900}s_b^{900} - \sum_{b=1}^{N\_cells\_900} l_{kb}^{900}s_b^{900}(\delta Q_b^{-1})^{1800,C} \tag{24}$$

and

$$(\tilde{d}_k^D)^{1800} = \left\langle \frac{t_k}{Q_k}\right\rangle^{1800} - d_k^D - Q_T^{-1}\sum_{b=1}^{N\_cells\_900} l_{kb}^{900}s_b^{900} - \sum_{b=1}^{N\_cells\_900} l_{kb}^{900}s_b^{900}(\delta Q_b^{-1})^{1800,D} \tag{25}$$

where $(\delta Q_b^{-1})^{1800,C}$ and $(\delta Q_b^{-1})^{1800,D}$ are respectively the solutions obtained with the CN method and the SD method for 1800 m side blocks and that where assigned to the *N_cells_*900 blocks of 900 m side crossed by the *k* th ray. In the SD method the constant value $\langle(t_k/Q_k)\rangle^{1800}$ has also been updated with the informations obtained in the previous step. The inversion problem becomes, for a resolution of 900 m:

$$(\tilde{d}_k^{C,D})^{1800} = \sum_{b=1}^{N\_cells\_900} G_{kb}^{900}[(\delta Q_b^{900})^{-1}]^{C,D} \tag{26}$$

where the superscript 900 stands for the step of the grid and the $(\delta Q_b^{900})^{-1}$ are the inverse variations respect the inverse quality factor of the 1800 m cube in which they are contained. The elements

of the inversion matrix, G^{900}_{kb}, are the length of the k th ray segment in the 900-m side b th block l^{900}_{kb} multiplied for his slowness s^{900}_{b}:

$$G^{900}_{kb} = l^{900}_{kb} s^{900}_{b} \tag{27}$$

where we consider only blocks crossed by at least $n_R = 17$ rays see Eq. (14). The inversion is linear and we can constrain the average of the $(\delta Q^{900}_b)^{-1}$ to be zero. The inverse quality factor of each 900 m block b is given by

$$(Q^{900}_b)^{-1} = Q_T^{-1} + (\delta Q^{1800}_b)^{-1} + (\delta Q^{900}_b)^{-1} \tag{28}$$

while the percentage reduction is 70% in residual.

C.4. Point 5: cell dimension of 300 m

The last step is achieved upgrading the data vectors writing the following two formulas:

$$(\tilde{d}^C_k)^{900} = \left\langle \frac{1}{2\pi f} \ln\left(\frac{1}{P(f,t_c)}\right)\right\rangle - d^C_k - Q_T^{-1} \sum_{b=1}^{N\_cells\_300} l_{kb} s_b - \sum_{b=1}^{N\_cells\_300} l_{kb} s_b (\delta Q_b^{-1})^{1800,C} - \sum_{b=1}^{N\_cells\_300} l_{kb} s_b (\delta Q_b^{-1})^{900,C} \tag{29}$$

and

$$(\tilde{d}^D_k)^{900} = \left\langle \frac{t_k}{Q_k}\right\rangle^{900} - d^D_k - Q_T^{-1} \sum_{b=1}^{N\_cells\_300} l_{kb} s_b - \sum_{b=1}^{N\_cells\_300} l_{kb} s_b (\delta Q_b^{-1})^{1800,D} - \sum_{b=1}^{N\_cells\_300} l_{kb} s_b (\delta Q_b^{-1})^{900,D} \tag{30}$$

where $(\delta Q_b^{-1})^{900,C}$ and $(\delta Q_b^{-1})^{900,D}$ are the solutions obtained in the previous steps that were assigned to a number of N_cells_300 blocks of 300 m side, crossed by the k th ray. As before, the constant value $\langle (t_k/Q_k)\rangle^{900}$ has been updated with the informations obtained in the previous steps. The inversion problem becomes

$$(\tilde{d}^{C,D}_k)^{900} = \sum_{b=1}^{N\_cells\_300} G^{300}_{kb} [(\delta Q^{300}_b)^{-1}]^{C,D} \tag{31}$$

where the superscript 300 stands for the grid step, and the elements of the inversion matrix, G^{300}_{kb}, are given by the length of the k th ray segment in the b th block, l^{300}_{kb}, multiplied for his slowness s^{300}_b:

$$G^{300}_{kb} = l^{300}_{kb} s^{300}_b \tag{32}$$

applying Eq. (14), we consider only blocks crossed by at least $n_R = 5$rays. The percentage reduction in residual is 94%. The inverse quality factor of each 300 m block b is given by

$$(Q^{300}_b)^{-1} = Q_T^{-1} + (\delta Q^{1800}_b)^{-1} + (\delta Q^{900}_b)^{-1} + (\delta Q^{300}_b)^{-1} \tag{33}$$

References

Andronico, D., Calderoni, G., Cioni, R., Sbrana, A., Suplizio, R., Santacroce, R., 1995. Geological map of Somma–Vesuvius Volcano. Per. Mineral. 64, 77–78.

Aki, K., 1980. Attenuation of shear-waves in the lithosphere for frequencies from 0.05 to 25 Hz. Phys. Earth Planet. Int. 21, 50–60.

Auger, E., Gasparini, P., Virieux, J., Zollo, A., 2001. Seismic evidence of an extended magmatic sill under Mt. Vesuvius. Science 294, 1510–1512.

Bai, C., Greenhalgh, S., 2005. 3D multi-step travel time tomography: imaging the local, deep velocity structure of Rabaul volcano, Papua New Guinea. Phys. Earth Planet. Int. 151, 259–275.

Berrino, G., Coppa, U., De Natale, G., Pingue, F., 1993. Recent geophysical investigation at Somma–Vesuvius volcanic complex. J. Volcanol. Geotherm. Res. 58, 239–262.

Bianco, F., Castellano, M., Milano, G., Ventura, G., Vilardo, G., 1997. The Somma–Vesuvius stress field induced by regional tectonics: evidences from seismological and mesostructural data. J. Volcanol. Geotherm. Res. 82, 199–218.

Bianco, F., Castellano, M., Del Pezzo, E., Ibanez, J.M., 1999. Attenuation of short period seismic waves at Mt. Vesuvius, Italy. Geophys. J. Int. 138, 67–76.

Block, L.V., 1991. Joint hypocenter-velocity inversion of local earthquakes arrival time data in two geothermal regions. Ph.D. dissertation, M.I.T., Cambridge.

Capuano, P., Gasparini, P., Zollo, A., Virieux, J., Casale, R., Yeroyanni, M., 2003. The internal structure of Mt. Vesuvius. A seismic tomography investigation. Liguori Editore, ISBN: 88-207-3503-2.

Chiodini, G., Marini, L., Russo, M., 2001. Geochemical evidence for the existence of high-temperature hydrothermal brines at Vesuvio volcano, Italy. Geochem. Cosmochem. Acta 65 (13), 2129–2147.

Chouet, B., 1996. New methods and future trends in seismological volcano monitoring. In: Scarpa, R., Tilling, R.I. (Eds.), Monitoring and Mitigation of Volcano Hazards. Springer, Berlin, pp. 23–97.

Chouet, B., 2003. Volcano Seismology. Pageoph 160, 739–788.

Del Pezzo, E., Bianco, F., Saccorotti, G., 2004. Seismic source dynamics at Vesuvius volcano, Italy. J. Volcanol. Geotherm. Res. 133, 23–39.

Del Pezzo, E., Bianco, F., Zaccarelli, L., 2006a. Separation of Qi and Qs from passive data at Mt. Vesuvius: a reappraisal of seismic attenuation. Phys. Earth Planet. Int. 159, 202–212.

Del Pezzo, E., Bianco, F., De Siena, L., Zollo, A., 2006b. Small scale shallow attenuation structure at Mt. Vesuvius, Italy. Phys. Earth Planet. Int. 157, 257–268.

De Natale, G., Capuano, P., Troise, C., Zollo, A., 1998. Seismicity at Somma–Vesuvius and its implications for the 3D tomography of the volcano. In: Spera, F.J., De Vivo B., Ayuso R.A., Belkin H.E. (Eds.) J. Volcanol. Geotherm. Res., Special Issue Vesuvius. 82, 175–197.

De Natale, G., Troise, C., Pingue, F., Mastrolorenzo, G., Pappalardo, L., 2005. The Somma–Vesuvius volcano (Southern Italy): Structure, dynamics and hazard evaluation. Earth Sci. Rev. 74, 73–111.

Eberhart-Phillips, D., 1990. Three-dimensional P and S velocity structure in the Coalinga region, California. J. Geophys. Res. 95, 15343–15363.

Eberhart-Phillips, D., Reyners, M., Chadwick, M., Chiu, J.M., 2005. Crustal heterogeneity and subduction processes: 3-D V_P, V_P/V_S and Q in the southern North Island, New Zealand. Geophys. J. Int. 162, 270–288.

Galluzzo, D., Del Pezzo, E., Maresca, R., La Rocca, M., Castellano, M., 2005. Site effects estimation and source-scaling dynamics for local earthquakes at Mt. Vesuvius, Italy. Congress acts, ESG2006, Grenoble. Paper Num. 36.

Giampiccolo, E., Gresta, S., Ganci, G., 2003. Attenuation of body waves in Southeastern Sicily (Italy). Phys. Earth Planet. Int. 135, 267–279.

Gubbins, D., 2004. Time Series Analysis & Inverse Theory for Geophysicists. Cambridge University Press.

Gudmundsson, Ó., Finlayson, D.M., Itikarai, I., Nishimura, Y., Johnson, W.R., 2004. Seismic attenuation at Rabaul volcano, Papua New Guinea. J. Volcanol. Geotherm. Res. 130, 77–92.

Gusev, A.A., Abubakirov, I.R., 1999. Vertical profile of effective turbidity reconstructed from broadening of incoherent body-wave pulses. Geophys. J. Int. 136, 309–323.

Hansen, S., Thurber, C.H., Mandernach, M., Haslinger, F., Doran, C., 2004. Seismic velocity and attenuation structure of the east rift zone and South Flank of Kilauea Volcano, Hawaii. Bull. Seism. Soc. Am. 94, 1430–1440.

Ito, H., DeVilbiss, J., Nur, A., 1979. Compressional and shear waves in saturated rock during water–steam transition. J. Geophys. Res. 84, 4731–4735.

Lomax, A., Zollo, A., Capuano, P., Virieux, J., 2001. Precise absolute earthquake location under Somma–Vesuvius volcano using a new three-dimensional velocity model. Geophys. J. Int. 146, 313–331.

Marianelli, P., Métrich, N., Sbrana, A., 1999. Shallow and deep reservoirs involved in magma supply of the 1944 eruption of Vesuvius. Bull. Volcanol. 61, 48–63.

Mulargia, F., Tinti, S., 1985. Seismic sample areas defined from incomplete catalogues; an application to the Italian territory. Phys. Earth Planet. Int. 40, 273–300.

Nava, A.F., Garcìa-Arthur, R., Castro, R.R., Suàrez, C., Màrquez, B., Nùñez-Cornù, F., Saavedra, G., Toscano, R., 1999. S wave attenuation in the coastal region of Jalisco-Colima, México. Phys. Earth Planet. Int. 115, 247–257.

Sambridge, M.S., Gudmundsson, O., 1998. Tomographic systems of equation with irregular cells. J. Geophys. Res. 103, 773–781.

Santacroce, R., 1987. Somma–Vesuvius. CNR, Quaderni di Ricerca Scientifica.

Sato, H., Fehler, M.C., 1998. Seismic Wave Propagation and Scattering in the Heterogenous Earth. Springer.

Scarpa, R., Tronca, F., Bianco, F., Del Pezzo, E., 2002. High resolution velocity structure beneath Mount Vesuvius from seismic array. Geophys. Res. Lett. 29 (21), 2040.

Schurr, B., Asch, G., Rietbrock, A., Trumbull, R., Haberland, C., 2003. Complex patterns of fluid and melt transport in the central Andean subduction zone revealed by attenuation tomography. Earth. Planet. Sci. Lett. 215, 105–119.

Sengupta, M.K., Rendleman, C.A., 1989. Case study: the importance of gas leakage in interpreting amplitude-versus-offset (AVO) analysis. Soc. Explor. Geophys. Abstracts 59, 848–850.

Spencer, J., 1979. Bulk and shear attenuation in Berea sandstone: the effects of pore fluids. J. Geophys. Res. 84, 7521–7523.

Thurber, C.H., 1987. Seismic structure and tectonics of Kilauea volcano Hawaii. In: Decker, R.W., Wright, T.L., Stauffer, P.H. (Eds.), Volcanism in Hawaii. US Geological Survey, pp. 919–934.
Tondi, R., De Franco, R., 2003. Three-dimensional modeling of Mount Vesuvius with sequential integrated inversion. J. Geophys. Res. 108, 2256.
Um, J., Thurber, C.H., 1987. A fast algorithm for two-point seismic ray tracing. Bull. Seism. Soc. Am. 77, 972–986.
Wegler, U., 2003. Analysis of multiple scattering at Vesuvius volcano, Italy, using data of the Tomoves active seismic experiment. J. Volcanol. Geotherm. Res. 128, 45–63.
Zollo, A., D'Auria, L., De Matteis, R., Herrero, A., Virieux, J., Gasparini, P., 2002. Bayesian estimation of 2-D *P*-velocity models from active seismic arrival time data: imaging of the shallow structure of Mt, Vesuvius (Southern Italy). Geophys. J. Int. 151, 566–582.